

RESEARCH ARTICLE

10.1029/2017JA024648

Key Points:

- Electromagnetic fields across ocean-continent boundaries are solved via FDTD while accounting for a finite-depth ocean and topography
- Analytical approaches are found to provide a close approximation to the more realistic FDTD results for the range of studied scenarios
- Surface electric field enhancements are highly localized along the coast, even for low frequencies and shallow oceans

Correspondence to:

S. Pokhrel,
santosh_everest@yahoo.com

Citation:

Pokhrel, S., Nguyen, B., Rodriguez, M., Bernabeu, E., & Simpson, J. J. (2018). A finite difference time domain investigation of electric field enhancements along ocean-continent boundaries during space weather events. *Journal of Geophysical Research: Space Physics*, 123. <https://doi.org/10.1029/2017JA024648>

Received 3 AUG 2017

Accepted 26 APR 2018

Accepted article online 29 MAY 2018

A Finite Difference Time Domain Investigation of Electric Field Enhancements Along Ocean-Continent Boundaries During Space Weather Events

Santosh Pokhrel¹ , Bach Nguyen¹, Miguel Rodriguez¹, Emanuel Bernabeu², and Jamesina J. Simpson¹ 

¹Department of Electrical and Computer Engineering, University of Utah, Salt Lake City, UT, USA, ²PJM Interconnection, Audubon, PA, USA

Abstract Geomagnetic disturbances caused by solar storms have the potential to create large-scale geomagnetically induced currents in long conductors at the Earth's surface. These may disrupt the operation of electric power grids and cause blackouts. Ocean-continent boundary regions are of particular concern because of the sharp contrast between the higher ocean electrical conductivity compared to the lower continental conductivity. This contrast may generate high-amplitude geoelectric fields and cause power grids in coastal regions to be more vulnerable to space weather hazards. Previously, analytical calculations were used to estimate geomagnetically induced currents at ocean-continent boundaries. However, for the analytical equations to be solvable, the physics and geometries of the problem were simplified. As a result of these simplifications and due to a lack of published measurements examining this issue in coastal regions, it is difficult to know for sure whether there are unique hazards to electric power grids at ocean-continent boundaries. In this paper, a grid-based, time domain modeling approach is used to solve the complete Maxwell's equations, which permits accommodation of (1) the complete physics of the propagating electromagnetic fields from disturbed ionospheric currents through the air and into the lithosphere and even into the ocean via the skin effect and (2) more realistic coastal geometries. Using this more robust approach, in the variety of scenarios studied in this paper, only a local enhancement of the electric fields was observed, which are expected to only pose potential hazards to power grids only a local scale near ocean-continent boundaries.

1. Introduction

The Sun ejects an enormous amount of plasma and magnetic fields during coronal mass ejections. When directed toward the Earth, these charged particles and magnetic fields can interact with the Earth's magnetosphere and generate a geomagnetic storm (Kappenman, 2010). This increases the movement of plasma in the magnetosphere. Disturbed currents are also produced in the ionosphere (including ionospheric currents, ring current, and field-aligned currents) leading to a very complex distribution of currents all the way down to an altitude of ~100 km, where they are called enhanced polar electrojets and equatorial electrojets (Boteler & Pirjola, 1998). These disturbed currents can disrupt the electromagnetic fields at the Earth's surface, cause large geoelectric fields over large distances, and lead to geomagnetically induced currents (GICs) in long conductors and disruptions or even blackouts to electric power grids.

The largest geomagnetic storm on record occurred in 1859 (British Geological Survey, 2011; Carrington, 1859). That storm caused electric shocks to telegraph operators communicating over 100-km-long wirelines. As a result, business transactions requiring telegraphic exchanges were completely shut down in the world's major capitals (Odenwald, 2002). A 2008 U.S. National Academy of Sciences space weather report (National Research Council of the National Academies, 2008) indicates that extreme space weather events "though rare, are likely to occur again sometime in the future." However, a reoccurrence of an 1859-magnitude space weather (coronal mass ejection-driven geomagnetic) storm could disrupt modern society to a much greater degree than in 1859. An indication of this is the significantly smaller-scale March 1989 geomagnetic storm that caused the HydroQuebec power grid to fail for 9 hr, leaving six million customers without electricity and having an overall economic cost in the millions of dollars (Bolduc, 2002).

To study potential space weather hazards to electric power grids, electromagnetic fields at the surface of the Earth must be known. The amplitude of the horizontal geoelectric field and its spatial extent along the Earth's

surface is a primary factor that determines whether GICs will couple to a power transmission line or not. Another crucial factor is how robust the power transmission system is to GICs. Fundamentally, the amplitude of the surface geoelectric field may be predicted if the following is taken into account: (1) current behavior in the ionosphere (and ideally also the magnetosphere), (2) ionosphere-magnetosphere electrochemical dynamics, (3) the conductivity profile of the lithosphere, and (4) regional topography (i.e., proximity to oceans).

Multiple approaches have been previously used to estimate the electromagnetic fields at the Earth's surface due to ionospheric currents, including, for example, the Biot-Savart law (Pulkkinen et al., 2007), complex image theory (Pulkkinen et al., 2007), method of auxiliary sources (Shepard & Shubitidze, 2003), plane wave method (Viljanen et al., 2006), volume integral equation technique (Oijala et al., 2014), and the finite element method (Matandirotya et al., 2015). These approaches are particularly useful for studying surface electric fields (and GICs) over long time spans (on the order of minutes to hours), when infinite propagation speeds of the ionospheric currents can be assumed, and when the geometries can be assumed to be homogenous or highly simplified. (We note that although finite element method is capable of modeling sophisticated geometries, the work of Matandirotya et al., 2015, simulated only a 2-D layered geometry and assumed an incident plane wave).

Of particular interest in this paper is the behavior of surface electromagnetic fields (and GICs) near ocean-continent boundaries during geomagnetic storms. Ocean-continent boundaries have the potential to pose unique hazards during geomagnetic storms to electric power grids located in the vicinity of a coastline. The sharp contrast in the electrical conductivity between the ocean electrical conductivity (~ 3 or 4 S/m, depending on salinity and temperature) and the continent (on the order of 0.1 or 0.001 S/m) can generate large geoelectric fields between the two regions. As a result, large currents may flow in the relatively low-conductivity ground near ocean-continent boundaries. This could result in large GICs flowing in any overlying conductors.

A number of publications have included the general physics of GICs in coastal regions (e.g., Beamish et al., 2002; Bailey & Edwards, 1976; Chan et al., 1981; Dosso et al., 1980; Edwards et al., 1971; McKay, 2004; Miles & Dosso, 1980; Torta et al., 2017) or on a global scale (e.g., Olsen & Kuvshinov, 2004; Püthe et al., 2014). These papers have greatly advanced our understanding of geomagnetic hazards; however, they did not examine electric field variations along realistic coastline geometries at high resolutions. A high-resolution model is extremely important along the coast, since there may be an amplification of the electric fields within a certain distance inland.

Several publications have addressed the unique physics of GICs specifically at ocean-continent boundaries (e.g., Gilbert, 2005, 2014; Pirjola, 2013). In these papers, electromagnetic fields are calculated for a homogeneous coastal slope. None of these papers have accounted for actual coastal geometries (for example, a sloping region followed by a finite depth ocean).

The thin sheet model (Vasseur & Weidelt, 1977) is widely used by GIC communities to investigate GIC effects on various infrastructures (e.g., Bailey et al., 2017; Beggan et al., 2013; Dawson & Weaver, 1979; Green & Weaver, 1978; Thomson et al., 2005). This model can solve a 3-D quasi-static induction problem, especially in areas with larger lateral heterogeneity (in terms of conductivity) on the surface. It also provides fast computations by solving only for the horizontal components of the electric field. This approach appears to be a good candidate for studying electric fields at realistic ocean-continent boundaries at higher resolutions that is typically used for inland studies (on the order of 3 km or less rather than tens of kilometers); however, to our knowledge, this has not yet been done.

Despite all of the above publications, there is still a limited understanding of the surface electromagnetic field behavior near ocean-continent boundaries. The issue of ocean-continent boundaries and whether they pose significant risks to power grids is important, and there are still unresolved issues. This paper serves to take a closer look at this issue using an established numerical technique (the finite difference time domain [FDTD] method). FDTD provides more rigorous (full-vector Maxwell's equations) solutions and provides the capability to account for intricate details of the Earth's topography and electrical variations in 3-D. Contrary to the thin sheet model and other approaches listed above, the FDTD method also solves wideband problems effectively within one simulation.

Specifically, the FDTD method (Taflov & Hagness, 2005; Yee, 1966) is used to calculate electromagnetic fields at the surface of the Earth near ocean-continent boundaries. Figure 1 illustrates an example FDTD grid cell in

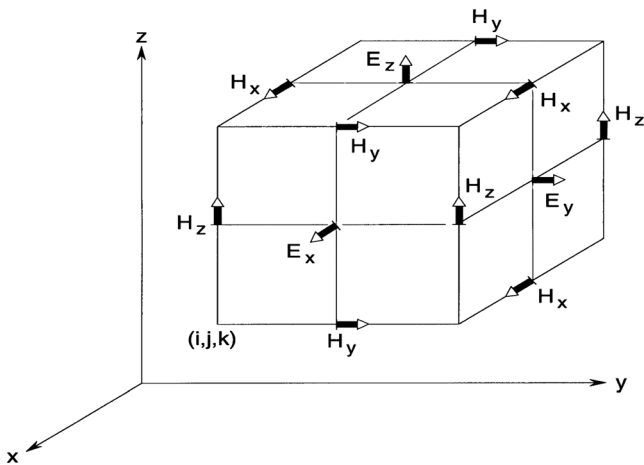


Figure 1. One grid cell of the 3-D FDTD model, illustrating the spatial positions of the six electric and magnetic field components (Yee, 1966).

3-D. The time-dependent Ampere’s and Faraday’s laws in partial differential form are discretized using central difference approximations to the time and space partial derivatives. The resulting finite difference equations are solved in a leapfrog manner: the electric field vector components (E_x , E_y , and E_z as shown in Figure 1) are solved at a given instant in time, and then the magnetic field vector components (H_x , H_y , and H_z in Figure 1) are solved one half time step later. This process repeats over a time span of interest.

As a time domain method, FDTD permits modeling of arbitrary source time-waveforms, variable current source orientations, and even the finite propagation velocity of the ionospheric currents. Further, as a grid-based method, FDTD permits modeling of complex geometries, such as sloping coastlines combined with finite depth oceans (rather than a coastline having a constant, infinitely long slope as in the previous analytical studies; e.g., Gilbert, 2014).

FDTD requires a relatively small time step (on the order of microseconds for kilometer-scale grid resolutions) in order to maintain stability. As a result, it is computationally demanding for GIC studies compared

to other approaches (e.g., induction equation or frequency domain approaches). Despite this, FDTD is used in the present paper to help the space weather community gain confidence in its validity and utility for GIC calculations. FDTD may provide a unique perspective since it is a time domain solution and solves the full-vector Maxwell’s equations. For example, FDTD may be used to study the recently discovered intense, short timescale (on the order of seconds or less) electric fields predicted and measured during space weather events (Clilverd et al., 2010; Pulkkinen et al., 2015; Simpson, 2011).

In this paper, the FDTD modeling approach is first validated for GIC calculations by comparing FDTD-calculated electromagnetic fields over a continent with the analytically calculated results presented in Boteler and Pirjola (1998). FDTD-calculated electromagnetic fields above an ocean are also provided. Next, electromagnetic fields at ocean-continent boundaries are studied, including the effects of different ocean depths, lithosphere conductivities, ionospheric source frequencies (including a pulse), and ionospheric current source orientations. Finally, future FDTD modeling possibilities are discussed.

2. Comparison With an Analytical Result

Appendix A provides an overview of FDTD and the FDTD modeling techniques used to obtain the results provided in this paper. First, FDTD results for calculated surface electric fields are compared with analytical results. Specifically, FDTD-calculated surface electromagnetic fields are compared with the analytical results presented in Boteler and Pirjola (1998). The electrical conductivity layering of Quebec shown in Figure 2 is modeled in a 2-D FDTD grid along with an infinitely long ionospheric current source at an altitude of 100 km above the surface of the Earth. A 2-D FDTD grid is used to exploit the symmetry of the problem. A sinusoidal source of frequency 0.003 Hz (time period: 5 min) and current magnitude of 1 million amperes is used. The current source is oriented along the x axis according to Cartesian right-hand coordinate system. The top and two sides of the model are terminated by a convolutional perfectly matched layer (CPML) absorbing boundary condition (see Appendix A for more information) that is 100 cells thick. The bottomside of the grid is terminated by a surface impedance boundary condition (SIBC; see Appendix A for more information) at a depth of four skin depths. A grid resolution of 10 km (horizontally, in the y direction) \times 5 km (vertically, in the z direction) is utilized. Initially, the ionosphere is ignored (free space is assumed

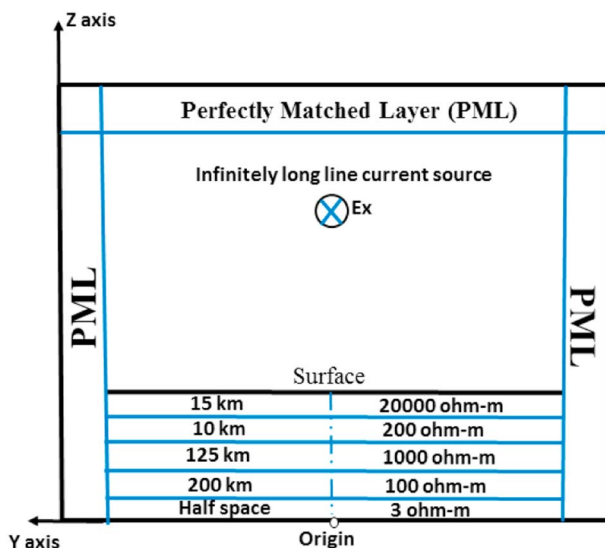


Figure 2. 2-D FDTD model geometry with lithosphere resistivity structure for Quebec (Boteler & Pirjola, 1998).

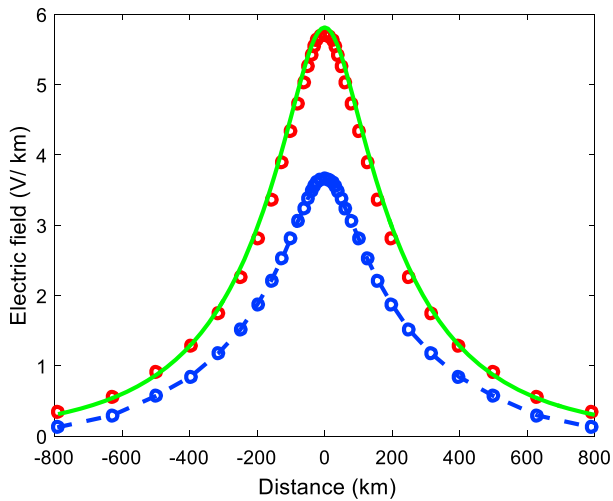


Figure 3. Comparison of the electric field amplitude oriented along the x -direction (E_x) and sampled along the y direction (see Figure 2) obtained via FDTD (green line) and analytically as calculated in (Boteler & Pirjola, 1998; red line) for a free-space ionosphere. The infinite current line source is positioned 100 km above the ground at 0 km. The blue curve is the FDTD result for an analogous scenario but including the lower ionosphere/upper atmosphere conductivity profile.

above the ground) in this simulation to match the scenario of Boteler and Pirjola (1998).

Since FDTD is a time domain method, the sinusoidal source must be turned on at the beginning of the simulation (time, $t = 0$). Typically, FDTD simulations are time-stepped out several periods in order to achieve steady state amplitudes for comparison with frequency domain analytical results. However, since the periods (wavelengths) of interest are so long relative to the FDTD time step increment (14.75 μ s), the FDTD solution reaches steady state within the first period of the simulation. This has been confirmed by running the simulation longer to see that the results do not change for longer periods of time.

The electric field along the surface of the Earth is sampled. As shown in Figure 3, the sampled FDTD-computed electric field agrees very strongly with the exact analytical results of Boteler and Pirjola (1998). There is a maximum 1.99% difference observed between the two curves at 0 km (directly below the source). This difference is due to the extra thick absorbing boundary condition along the edges of the model (see Appendix A) used in the FDTD model compared to the analytical model (which does not need an absorbing boundary). Similar agreement was also observed for the other field components when compared to the analytical results of Boteler and Pirjola (1998).

FDTD can account for varying materials and geometries in a straightforward manner, so also shown in Figure 3 is the case wherein the lossy ionosphere is included. The ionosphere would be expected to attenuate any electromagnetic wave propagating toward the Earth's surface because the lower ionosphere and upper atmosphere is a lossy medium. At the low frequencies of interest in this paper, the ionosphere is approximated as an exponential conductivity profile that varies with altitude (Bannister, 1985). This profile has been used in the past in analytical calculations (e.g., Bannister, 1985) and in global FDTD simulations (Simpson & Taflove, 2004), both of which yielded electromagnetic field values that compared well with measurements. As seen in Figure 3, including a homogeneous ionosphere conductivity profile is found to reduce the electromagnetic field amplitude at the Earth's surface by about 40% compared to case wherein the region above the Earth's surface is assumed to be free space. Note that all of the previous analytical studies of GICs at ocean-continent boundaries mentioned in section 1 treated the ionosphere as free space (i.e., ignored the presence of the ionosphere). The equivalent source currents assumed in the previous studies should generate a similar electric field response at the Earth's surface as when the actual currents are modeled in combination with a realistic ionosphere.

3. Field Strengths Over the Ocean

Electromagnetic field values are also calculated over an ocean half-space (note that more realistic ocean depths are considered in the following sections). The geometry of Figure 2 is modeled but with the Quebec lithosphere replaced by an ocean conductivity (3.3 S/m). The ocean is modeled to a depth of four skin depths for a source frequency of 0.003 Hz (each skin depth is ~ 4.7 km), and the bottom of the grid is again terminated by a SIBC. To obtain sufficient accuracy using FDTD, the grid resolution must be set such that there are at least about 10 grid cells per wavelength within every material of interest. Since the highly conductive seawater shortens the electromagnetic wavelength significantly compared to the Quebec lithosphere layering, a higher resolution grid (compared to the simulation in section 2) is needed to account for the reduced wavelength and skin depth. A grid resolution of 3 km (horizontally, in the y direction) \times 1.25 km (vertically, in the z direction) is used. A thick CPML of 1 Mm (333 cells) terminates the grid on the left and right sides (in the $\pm y$ directions).

Figure 4 (left) illustrates the FDTD-calculated electric field amplitude oriented along the x direction (E_x) and sampled along the y direction at the surface of the ocean with an ionosphere included. The peak field strength at 0 km (directly below the source) is around 0.226 V/km, which is significantly reduced from the

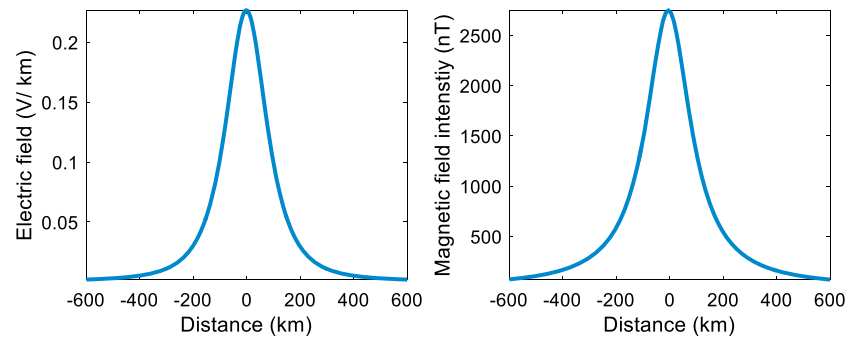


Figure 4. (left) FDTD-calculated electric field amplitude oriented along the x direction (E_x) and sampled along the y direction at the surface of the ocean. (right) FDTD-calculated magnetic field intensity oriented along the y -direction (B_y) and sampled along the y direction at the surface of the ocean.

lithosphere case of Figure 3 (roughly 5.8 V/km). The distance between the e^{-1} values to either side of the peak amplitude obtained at the center of the grid is ~ 240 km. Although relatively low in amplitude, the electromagnetic field values at the surface of the ocean constitute geomagnetic noise that can disturb marine instruments and naval operations (Kraichman, 1977).

Figure 4 (right) illustrates the magnetic field component oriented along the y direction and sampled along the y direction along the surface of the ocean. The peak B_y is $\sim 2,600$ nT at 0 km (directly below the source). The magnetic field intensity oriented in the z direction is of smaller amplitude (max of ~ 75 nT) at the surface of the ocean (not shown).

4. Ionospheric Currents Perpendicular to Ocean-Continent Boundaries

In this section, fully 3-D and symmetrical 3-D FDTD models are used to predict the electromagnetic fields at the Earth’s surface along ocean-continent boundaries wherein the ionospheric currents are oriented perpendicular to the coast. Figure 5 illustrates an example geometry with the ionospheric current extending vertically (radially) downward, horizontally across, and then vertically (radially) back upward again. Since the skin depth of the electromagnetic wave in the lithosphere is larger than that in the ocean, the FDTD models extend below the surface of the Earth to a depth of one skin depth for the lithosphere (~ 100 km), at which point it is terminated by an SIBC. The sides of the grid in the horizontal direction are terminated via a thick PML as in sections 2 and 3.

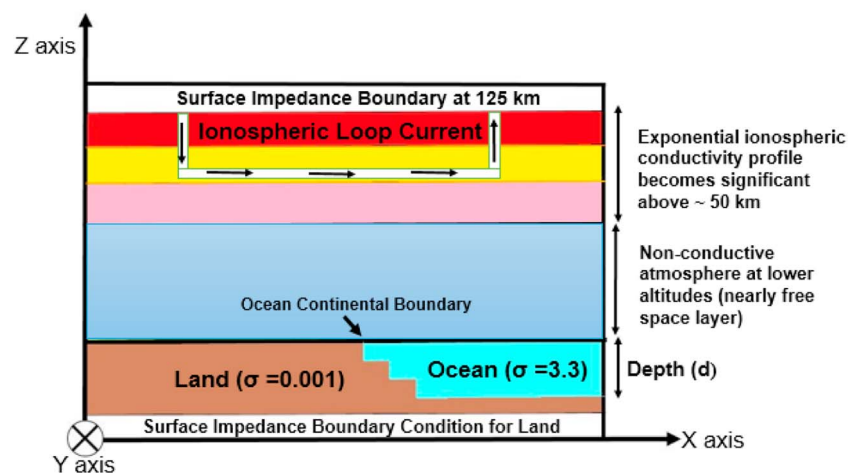


Figure 5. Ocean-continent boundary geometry. The slope of the transition from the continent to the ocean is 1/30 (1 m down for every 30 m horizontally toward the ocean). Since the grid resolution within the ocean is $dx = 3$ km and $dz = 1.6$ km, the slope of the transition from the continent to the ocean is 1 cell down for every 16 horizontal cells. (Note: not drawn to scale.)

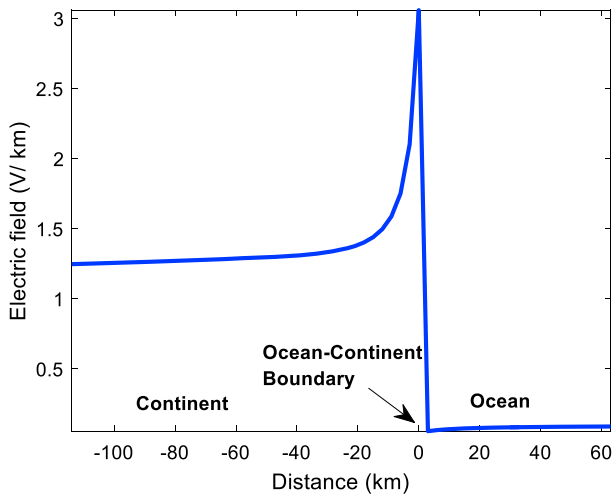


Figure 6. FDTD-calculated electric field oriented along the x -direction (E_x) and sampled along the x direction along the surface of ocean (located at distances >0 km) and along the surface of continent (located at distance ≤ 0 km). The coast is located at 0 km.

As seen in Figure 5, an exponential conductivity profile is used to model the ionosphere (see section 3; Bannister, 1985). Note that the lower atmosphere (below ~ 50 km) has almost negligible conductivity values (Nickolaenko et al., 2016). The grid extends to an altitude of 125 km above sea level, where it is terminated by an SIBC. At 125 km, the ionosphere is a good conductor, and so the SIBC effectively mirrors the current loop that extends below it. This mirroring yields a complete current loop, ensuring continuity of current. We note that the currents above 125 km would realistically extend much higher in altitude, but the currents closest to the Earth are expected to have the largest impact on the electromagnetic fields along the Earth's surface.

Other studies (e.g., Hakkinen et al., 1989) also assumed a current source that traveled horizontally over a finite distance. To be conservative, the source is assumed to be 1,000 km long horizontally and centered in the x direction at the boundary between the ocean and continent (the electrojet is typically several thousand kilometers long as it stretches around the nightside portion of the planet). Shorter sources yielded smaller electric fields at the coast. The source is oriented perpendicular to the ocean-continent boundary in order to study the maximum electric fields that may be obtained at the boundary due to the source

orientation. Figure 5 shows the source traveling from left to right; however, comparing different simulation results, a current source traveling from left to right versus right to left yielded the same maximum electric fields at the Earth's surface.

4.1. Results for a Sinusoidal Source at 0.003 Hz

A 3-D FDTD model is used to model a loop current source at a frequency of 0.003 Hz and down to an altitude of 100 km assuming the geometry shown in Figure 5. A variable grid resolution is used, which attains a maximum resolution in the seawater of $dx = 3$ km, $dy = 3$ km, and $dz = 1.6$ km. The depth of the ocean is set to 4.8 km. The amplitude of the source is 1 million amperes. Figure 6 illustrates the horizontal electric field (E_x , parallel to the ionospheric source current) obtained inland from the ocean-continent boundary where electric power grids may be located (0 km is directly at the ocean-continent boundary). There is an exponential decay of the fields inland from the coast, after which the decay is more gradual. This observed behavior agrees with the previous analytical observations in Gilbert 2014). Specifically, for the case of Figure 6, elevated fields are observed near the coast, but the fields decay to the e^{-1} value of the maximum at an inland distance of ~ 31 km. The horizontal electric fields perpendicular to the coast (E_y) are not plotted because their amplitudes are in the negligible mV/km range because the source is only on E_x and the geometry is homogeneous in the y direction.

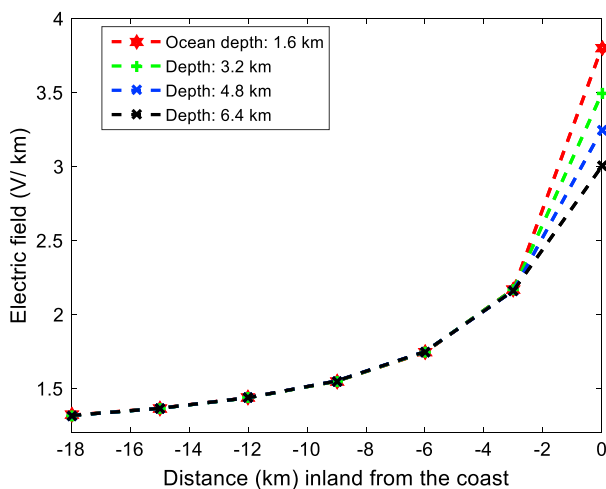


Figure 7. FDTD-calculated electric field oriented along the x direction (E_x) and sampled along the x direction inland from the coast (located at 0 km) for different ocean depths.

4.2. Effect of Different Ocean Depths

The modeling scenario of Figure 5 is repeated using different ocean depths. In our models, we do not include any sediments between the water and hard rock that may be up to several kilometers thick. To reduce the computational burden, symmetrical 3-D FDTD models are used. As seen in Figure 7, shallower oceans lead to higher electric fields at the coast. Another view of this is shown in Figure 8, which illustrates that the electric field at the surface of the continent immediately adjacent to the coastline increases when the depth of the ocean is decreased, but there is an abrupt change when the ocean is removed (0 km ocean depth case) compared to having a very thin ocean present. In other words, the surface electric field along the coast is inversely proportional to the depth of the ocean. A surface electric current singularity is expected to be generated near the edge of a conducting plate

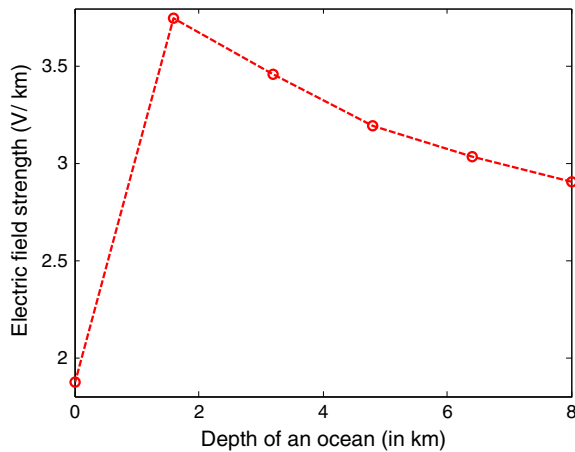


Figure 8. FDTD-calculated electric field oriented along the x direction (E_x) and sampled immediately adjacent to the coast above the continent for different ocean depths. Results are shown for ocean depths of 0, 1.6, 3.2, 4.8, 6.4, and 8 km.

(ocean in this case) when it is illuminated by an electromagnetic wave polarized with its electric field parallel to the edge. By the tangential magnetic field boundary condition at a conducting surface, this yields a tangential magnetic field singularity near the edge of the conducting ocean surface. In the case of Figures 7 and 8, it appears that the tangential magnetic field singularity is also influencing the tangential electric field at the edge of the ocean. (Note that the results in Figure 8 correspond to the maximum values attained on the right-hand side of Figure 7 for different ocean depths.)

4.3. Effect of Different Lithosphere Conductivity Values

Next, the lithosphere conductivity values are varied while keeping the ocean at a constant depth of 4.8 km. The results are shown in Figure 9. Lower lithosphere conductivity values lead to a larger discontinuity of the electrical conductivity at the ocean-continent boundary. As seen in Figure 9, this large conductivity discontinuity leads to larger variations (larger peaks and slower decays) in the electric fields inland from the coast.

4.4. Results for a Current Pulse Covering a Range of Frequencies

In this section, an advantage of FDTD is demonstrated: arbitrary source waveforms can be utilized in FDTD grids, and these models can thus provide results over a range of frequencies of interest from a single simulation. For example, setting the ocean to a depth of 4.8 km and the lithosphere conductivity to 0.001, the source (previously a sinusoid) is changed to a Gaussian-modulated sinusoidal source waveform. The source time-waveform is shown in Figure 10a and its spectrum in Figure 10b. As shown in Figure 10b, the pulse is centered at 0.05 Hz and spans from about 0.03 to 0.07 Hz (corresponding to time periods of 14.2 to 33.3 s). The frequency range was arbitrarily chosen to show the effect of the source frequency on the electric field behavior at the surface of the Earth.

The electric fields at the surface of the Earth are sampled in time until the pulse decays to zero at each observation point along the surface of the Earth. Figure 11 illustrates the electric field inland from the coast after taking the discrete Fourier transform of the sampled time-waveforms to obtain the amplitudes at different frequencies. Lower frequencies are seen to extend further inland than higher frequencies. Observing the difference between the 14-s and 5-min period results of Figure 11, it is expected that at sufficiently low frequencies (time periods longer than 5 min), the electric fields will be sufficiently elevated at large enough distances

from the coast to pose a local risk to electric power grids. However, note in Figure 11 that almost doubling the period of the wave (from 14 to 25 s) did not result in much of a change in the horizontal extent of the elevated electric fields near the coast.

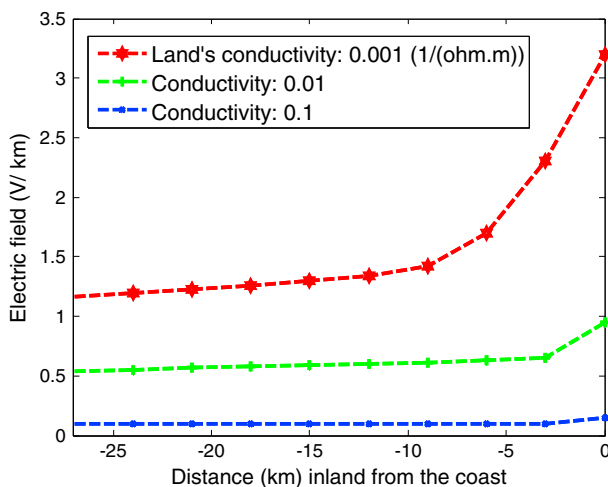


Figure 9. FDTD-calculated electric field oriented along the x -direction (E_x) and sampled along the x -direction inland from the coast (located at 0 km) for different lithosphere conductivities.

5. Ionospheric Currents Parallel to Ocean-Continent Boundaries

All of the previous studies considered ionospheric currents oriented perpendicular to the coast. In order to consider all possible scenarios that may lead to hazards to electric power grids, the 2-D FDTD model used in section 2 of this paper is altered to include a coastal geometry as seen in Figure 12. The ionosphere is neglected so that the results can be directly compared with the amplitude obtained in Figure 3. The grid is terminated by a thick PML in the x direction and on the top ($+z$) side; it is terminated by an SIBC on the bottom.

Figure 13 illustrates the electric field sampled along the Earth's surface for the geometry of Figure 12. Figure 13 shows that smaller amplitudes are observed when the ocean coast is present compared to when there is no ocean (there is only lithosphere). This is likely due to the electric

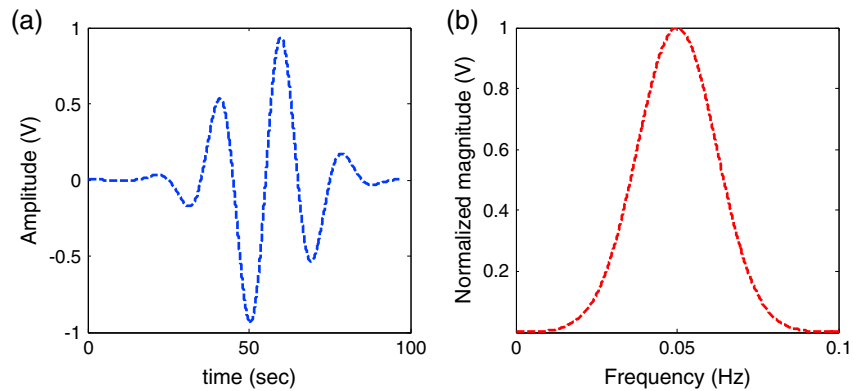


Figure 10. (a) Gaussian-modulated sinusoidal source waveform and (b) its corresponding spectrum.

field being influenced by the underlying local average conductivity within a certain distance perpendicular to the coast (the surface electric field is influenced by a spatially averaged conductivity value of the underlying ground/ocean). Earlier, it was observed in Figure 3 that a low lithosphere conductivity leads to a high surface electric field amplitude. Conversely, it was observed in Figure 4 (left) that a high conductivity ocean water leads to a low surface electric field amplitude. Thus, for the geometry of Figure 12, a local averaging of the underlying conductivities near the coastline raises the effective conductivity (compared to the lithosphere-only case). This reduces the surface electric fields in that region. In Figure 13, since the electric fields near the coastline are reduced due to the presence of the ocean, ionospheric currents oriented parallel to the coast are, in general, not expected to pose a threat to power grids.

6. Coastal Modeling of the North-Western United States

Modeling more realistic ocean-continent scenarios using FDTD is a matter of assigning different grid cells specific material parameters (conductivity and permittivity) depending on the position of the grid cell (within an ocean, lithosphere, or atmosphere region). As a test case, the north-western coast of the United States spanning from 43° to 49° (latitude) and 117°W to 129°W (longitude) is modeled. High-resolution global topography/bathymetry data (ETOPO1 Bedrock, cell-registered, xyz) provided by the National Geophysical Data Center are projected at a resolution of 3 km (matching the grid resolution) into a 3-D FDTD model (adapted from the model of Figure 5). Figure 14 shows the contour plot of the coastal topography that is modeled in the 3-D FDTD grid.

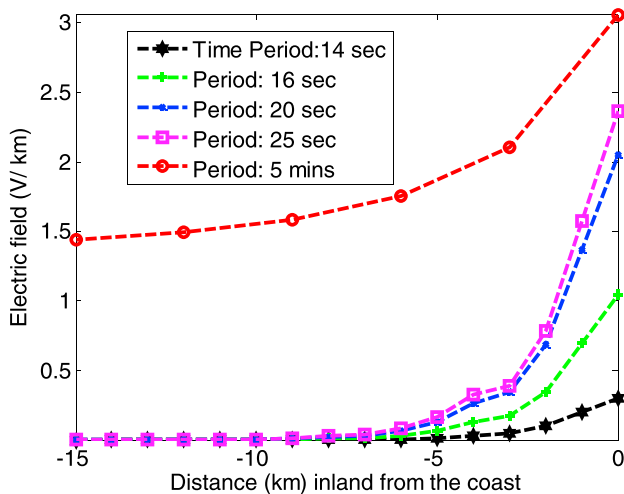


Figure 11. FDTD-calculated electric field oriented along the x-direction (E_x) and sampled along the x-direction inland from the coast (located at 0 km) for different source frequencies. The electric field for time period of 5 min is used from Figure 6.

A realistic conductivity composition of the continent is obtained from U.S. Geological Survey (Fernberg, 2012). Four different conductivity data sets are modeled in their respective regions of the grid: (1) Pacific Border (Willamette valley), (2) Pacific Border (Puget Lowlands), (3) Cascade-Sierra Mountains, and (4) Columbia Plateau. Conductivity data for under the Pacific Ocean are obtained from Hermance (2013), which corresponds to average conductivity values around the Pacific Ocean. The source is an ionospheric electrojet flowing perpendicular to the coastline (in the east-west direction) with a Cauchy (amplitude variation) distribution parallel to the coastline (Boteler et al., 1999). The Cauchy distribution has the form $j(y) = \left(\frac{l}{\pi}\right) \frac{a}{a^2 + y^2}$ parallel to the coast, where $l = 10^6$ A, $a = 25$ km (assumed here) and y is the distance from the center of the source. In the above expression, “ a ” refers to the half width at half maxima, or where the current amplitude is reduced by one half. The same boundary condition, ionosphere, and source frequency are used as in the previous 3-D modeling (Figure 5).

Figure 14a shows the ocean-continent topography/bathymetry variation along certain latitude and longitude on north-western coast of

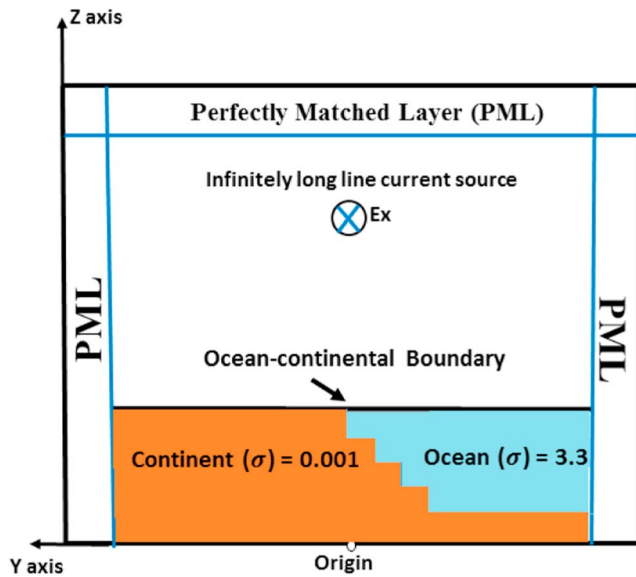


Figure 12. 2-D FDTD model geometry for the case of an ionospheric current oriented parallel to the coastline. The bottom of the grid is terminated by an SIBC. Since the resolution within the ocean is $dy = 3$ km and $dz = 1.6$ km, the slope of the transition from the continent to the ocean is 1 cell down for every 16 horizontal cells. (Note: not drawn to scale.)

different electrical conductivity and permittivity values. As a result, more realistic ocean geometries were modeled using FDTD than previously possible using analytical formulations. Different ocean depths, lithosphere conductivities, and source frequencies, as well as a varying topography and lithosphere composition scenario, were tested for ionospheric currents oriented perpendicular and then parallel to the coast.

FDTD modeling demonstrated that surface electric fields are enhanced near ocean-continent boundaries. However, these enhancements are highly localized to the coast. The enhancements extend farthest inland for three general scenarios:

1. Shallower oceans: there is an inverse relation between the coastal surface electric field amplitude and the ocean depth.

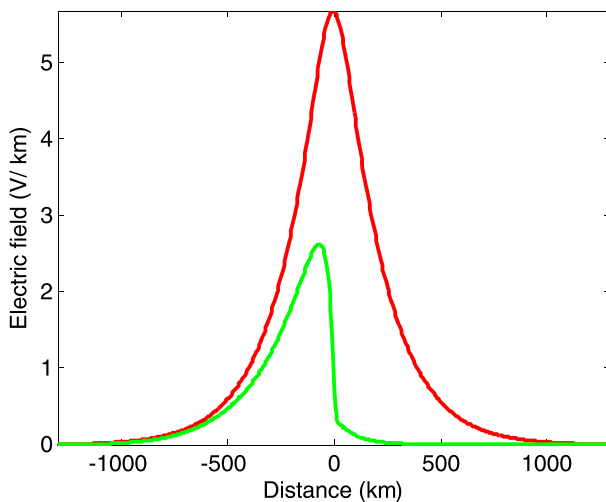


Figure 13. Comparison of the electric field amplitude oriented along the x direction (E_x) and sampled along the y direction for the case of an ionospheric current oriented parallel to the coast between the case with only lithosphere (red plot) and the case with ocean coast (green plot).

United States. The steady state tangential electric field at 0.003 Hz on the surface of coastal surface (as shown in Figure 14a) is shown in Figure 14b. The tangential electric field is observed at the ground surface (just above the ocean and just above the ground/mountains). The electric field polarized in the x direction (east-west direction) is most enhanced at the region where the slope of the bathymetry becomes less steep, at the coast, as well as by the mountains (where the topography and electrical conductivity changes). However, this enhancement decays very fast, which is accordance with the previous observations (see Figure 6). Note that the enhancements obtained at the coast are comparatively smaller than in the previous simulations (particularly Figure 6), since the source in this section involves a Cauchy distribution (the current is distributed over a larger region parallel to the coastline) rather than a line current.

7. Discussion

FDTD is a numerical technique that is straightforward to apply to complex geometries and material inhomogeneities. However, because it solves the complete Maxwell's equations, FDTD is computational intensive. Other analytical methods use simplified geometries and/or perform empirical data curve fitting in order to provide fast solutions. Using FDTD on the other hand, accounting for complex geometries and inhomogeneities is a matter of assigning individual grid cells different

electrical conductivity and permittivity values. As a result, more realistic ocean geometries were modeled using FDTD than previously possible using analytical formulations. Different ocean depths, lithosphere conductivities, and source frequencies, as well as a varying topography and lithosphere composition scenario, were tested for ionospheric currents oriented perpendicular and then parallel to the coast.

FDTD modeling demonstrated that surface electric fields are enhanced near ocean-continent boundaries. However, these enhancements are highly localized to the coast. The enhancements extend farthest inland for three general scenarios:

1. Shallower oceans: there is an inverse relation between the coastal surface electric field amplitude and the ocean depth.
2. Low conductivity lithosphere: the larger conductivity contrast between the continent and the ocean leads to a higher amplification of the fields.
3. Low-frequency ionospheric disturbances: for lower frequency ionospheric sources, the amplified fields extend slightly further inland.

For the three scenarios above, the electric field enhancements only extend a few more kilometers inland than for other cases (deeper oceans, higher conductivity lithospheres, and higher frequency ionospheric currents).

Power grids are designed to hold up against localized events, such as lightning strikes, hurricanes, fires, or weather events that may disrupt a small section of the grid (a small number of transformers). For an ocean-continent boundary to pose a distinct risk to electric power grids during a space weather event, high-amplitude electric fields would need to extend sufficiently inland from the coast (Ngwira et al., 2015), thereby disrupting a large number of transformers at different power grid stations. In other words, when high-amplitude electric fields extend over such a large region, they put at risk a large number of transformers—potentially, a larger number than the grid is typically designed to withstand (i.e., a larger number than a localized event

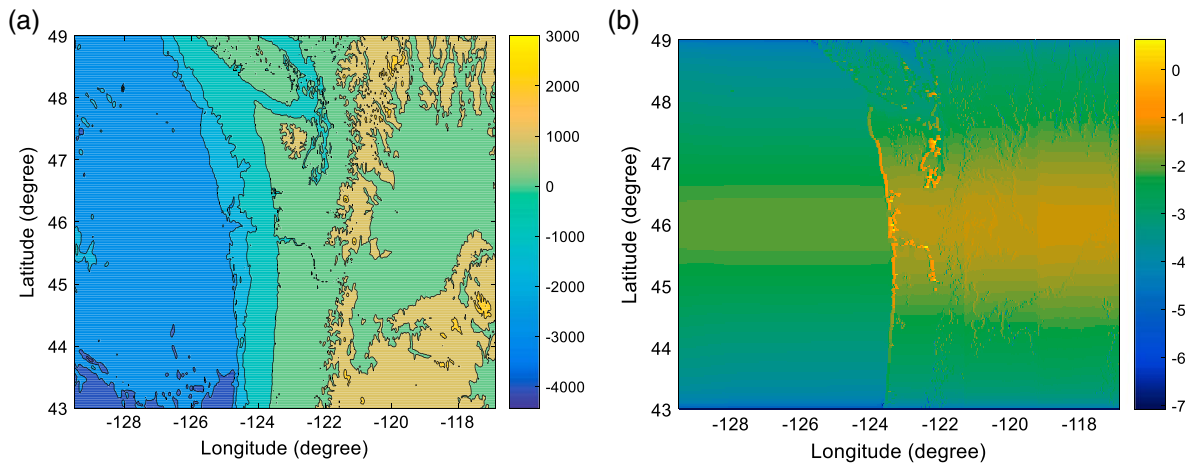


Figure 14. (a) Contour plot of the U.S. north-western coast topography according to NGDC data (in meters). (b) Tangential electric field (E_x) sampled for the topographical region shown on the left side of this figure. Note that the unit of electric field is log (V/km).

would impact). Since the FDTD modeling indicates that electric fields are amplified over only a relatively short distance from the coasts (as in Figure 6), it is expected that only a small fraction of transformers may be impacted in coastal regions. This coastal effect during a geomagnetic storm would represent a “localized event,” which power grids are designed to hold up against.

Thus, high conductivity contrasts at ocean-continent boundaries are not expected, in general, to pose a distinct threat to power grids and cause widespread blackouts. Certain power grid topologies and infrastructures that are located close to the coast, or on islands and peninsulas, might be more susceptible to ocean-continent boundary conditions; the proposed methodology can be used to assess the risk under such particular circumstances. We note that power grids on islands and along peninsulas are unique and may need to separately assess any special hazards in the coast regions.

When one or a few components of a power grid fail, it puts additional burden on the remaining components of the power grid. This can lead to a cascade of failures. Cascading failures of transformers have been reported in the literature during large geomagnetic storms (Kappenman, 2004). In this case, transformers at different substations may heat up and become saturated. If this results in cascading failures, the failures will likely not propagate systematically in the grid topologies, but rather propagate nonlocally (Hines et al., 2017). This means that the failure of a transformer at one station may not lead to the failure of its nearest neighbor, but instead the transformers at different geographic positions might fail. Therefore, the cascading propagation is a random phenomenon, which needs to be dealt with using a statistical approach such as an “influence graph” as reported in Hines et al. (2017). The authors would like to encourage a deeper study of this problem at ocean-continent boundaries, and in particular on islands and along peninsulas.

Ideally, more realistic ionospheric current source geometries would be modeled than line and sheet current sources. For example, realistic currents or electric fields predicted by the BATS-R-US model (Gombosi et al., 2000; Powell et al., 1999) or measured through AMIE (Richmond, 1992) may be directly modeled. Further, as part of future work, the ocean-continent boundary effects may be studied using a global FDTD model (Simpson & Taflove, 2004), which accounts for the Earth’s complete topography, oceans, ionosphere, and complex arrangement of ionospheric currents. The global FDTD-calculated surface electric fields could then be compared with measurement data at specific positions around the Earth, for example, those in Thomson et al. (2005) and Wei et al. (2013). Previously, this model was used to investigate short timescale electromagnetic fields over land (Simpson, 2011). Using global FDTD grids at resolutions on the order of $1 \text{ km} \times 1 \text{ km} \times 1 \text{ km}$ (these resolutions have already been simulated; Samimi & Simpson, 2016) ocean-continent boundary electromagnetic fields may be calculated while accounting for the complete Maxwell’s equations, realistic ionospheric currents, the Earth’s complete topography and bathymetry, the lithosphere conductivity inhomogeneities, and the global propagation of electromagnetic waves (which can circumnavigate the globe about seven times a second). Super-efficient global FDTD models will be needed, however, in order

to counter the long timescales of interest of GICs, since the global FDTD models use a time step increment on the order of microseconds and less.

Appendix A: Overview of the FDTD Models

FDTD provides solutions to the complete Maxwell's equations (Ampere's and Faraday's laws), including displacement currents (Taflove & Hagness, 2005; Yee, 1966). Using central differencing, the basic FDTD algorithm is second-order accurate in both space and time (Taflove & Hagness, 2005).

A1. Fully 3-D FDTD Model Description

Fully 3-D FDTD models permit variation of the coastal and source geometries in all three Cartesian directions. An example 3-D FDTD grid cell is shown in Figure 1. In 3-D, all six electric (E) and magnetic (H) field components are solved (E_x , E_y , E_z , H_x , H_y , and H_z). From Gilbert (2014), the electric fields at ocean-continent boundaries are expected to vary quickly with spatial position. Therefore, relatively high FDTD grid resolutions are used to investigate the ocean-continent effects on surface electromagnetic fields. Furthermore, the electromagnetic wavelength is reduced considerably within the ocean. Since FDTD requires at least 10 grid cells per wavelength throughout the grid, the grid resolution even higher in the ocean regions than the continent regions, on the order of 3000 m. Due to the different grid resolutions required in the ocean versus continent regions, a variable grid resolution is employed. Details about the variable grid resolution modeling approach are provided in the next section.

To ensure stability, the FDTD time step increment (dt) must satisfy the following relationship:

$$dt < \frac{1}{v} * \frac{1}{\sqrt{\left(\frac{1}{dx^2} + \frac{1}{dy^2} + \frac{1}{dz^2}\right)}} \quad (A1)$$

where dx , dy , and dz are the resolutions in the x , y , and z directions and v is the speed of the electromagnetic wave. Due to the small spatial resolution, the maximum dt values permitted in the simulations of this paper are on the order of microseconds. As a result, fully 3-D FDTD simulations of ocean-continent boundaries require long simulation times (a large number of time step iterations) in order to cover the long time spans of interest. The running times for the fully 3-D simulations average about four days using 256 processors.

To prevent unwanted reflections from the outside edges of the grid, the 3-D FDTD grid is terminated by a CPML (Roden & Gedney, 2000) in all four of the horizontal (x and y) directions. The two radial (vertical) directions of the grid are terminated by a monochromatic SIBC. These two boundary conditions are briefly described below.

A1.1. Variable Grid Resolutions

Variable gridding is used to reduce the computational burden of the FDTD models. The wavelength of the electromagnetic waves is greatly reduced in the oceans compared to the lithosphere and air regions. As a result, the wavelength of a 0.003 Hz electromagnetic wave (time period: 5 min.) is 10^8 km in air (free space) but just 31.8 km in an ocean, assuming a conductivity of 3.3 S/m. Further, the skin depth of the ocean at 0.003 Hz is ~ 5 km. In general, FDTD requires at least 10 grid cells per wavelength to ensure accurate solutions. Also, three cells are needed per skin depth to account for the rapid decay of the fields in the conducting material. As a result, larger grid cells can be used in the air region/lithosphere compared to the oceans. Variable gridding is used to increase the resolution in increments as the oceans are approached by a factor of 2 (for example, decreasing the grid cell sizes from 6 to 3 km). This approach has been successfully implemented previously in global FDTD modeling of remote sensing of oil fields in order to account more accurately for the topography of the Earth (Simpson & Taflove, 2006).

A1.2. Convolutional Perfectly Matched Layer (CPML) Boundary Condition

CPML (Roden & Gedney, 2000) is used to prevent reflections from the horizontal edges of the grids (x and y directions). CPML is a more advanced version of the original perfectly matched layer (PML) introduced in Berenger (1994). CPML thicknesses are typically about 10 cells for most FDTD simulations (on the order of about one-half wavelength thick), and reflections from the CPML are typically on the order of 10^{-4} and 10^{-5} . However, due to the very low frequencies (and correspondingly long wavelengths) studied in this

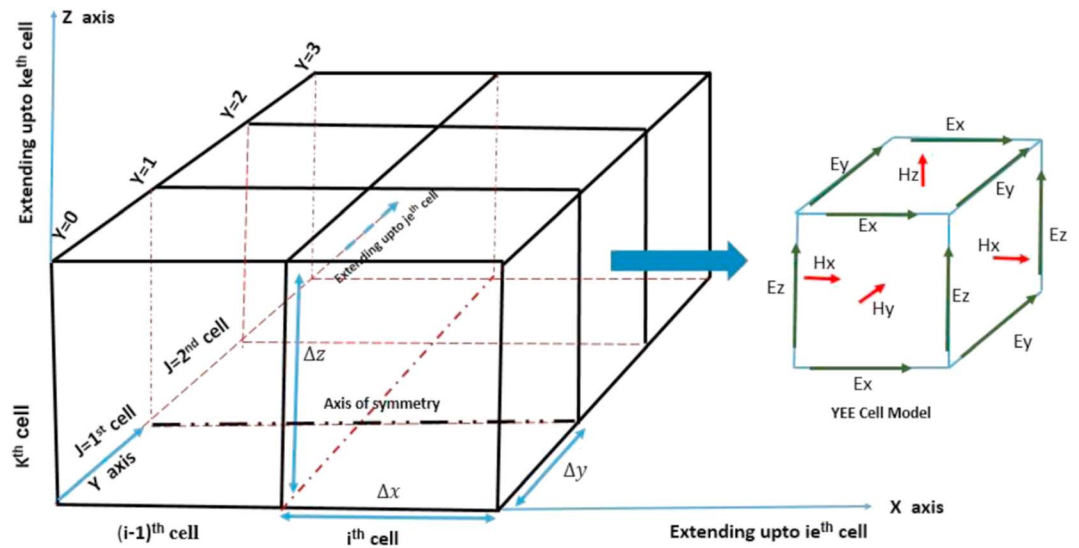


Figure 15. (left) Symmetrical 3-D FDTD model grid arrangement and (right) the positions of the six electric and magnetic field components within one grid cell of the model.

paper, a 10-cell-thick CPML is very thin relatively to a wavelength and the reflection is very high. As a result, a CPML that is on the order of 300 cells thick is used to better absorb the outgoing low-frequency electromagnetic waves.

A1.3. Surface Impedance Boundary Condition (SIBC)

SIBCs are typically used in FDTD grids to calculate the electromagnetic fields outside a lossy dielectric or conductor without having to model into its interior (Taflove & Hagness, 2005). This greatly reduces the computational burden because the FDTD grid then does not need to resolve the quickly decaying fields due to the skin effect. For an ocean-continent boundary, however, it is desirable to model into the conducting ground and ocean, but only so far as to account for the ocean-continent boundary geometries of interest and the large variation in electrical conductivity between the ocean and continent. As a result, an SIBC is implemented at a depth of four skin depths (on the order of 100 km below the Earth's surface), where the skin depth of the lithosphere is considered since the ocean skin depth is much smaller. In this case, the SIBC provides even more accurate compared to when it is used directly on the surface of an ocean or continent. By using an SIBC, the variation of the conductivities deeper into the lithosphere cannot be taken into account (they are instead approximated as a homogeneous value). However, we expect the largest effects of the electric fields at ocean-continent boundaries to be due to the more drastic ocean versus continent change in electrical conductivity rather than due to more subtle conductivity variations within the lithosphere.

The monochromatic SIBC formulation of Beggs et al. (1992) is used along the bottom edges of all of the FDTD models, and the top of all of the FDTD models that include the conductivity profile of the ionosphere. When included at the top of the grid, the SIBC is applied at an altitude of 125 km to approximate the continuation of the ionosphere. We note that as a result, the ionospheric currents do not extend vertically up through the entire ionosphere. However, the continuity of the currents is provided by the SIBC approximating the conductive ionosphere. Further, the disturbed ionospheric currents closest to the Earth as modeled in the FDTD grid are expected to influence the ground electromagnetic fields the most. For the lithosphere, the SIBC coefficients are calculated using the equations given in Sevgi et al. (2002). The SIBC is validated against brute-force modeling results (which involves extending the model deeper into the lithosphere until the electromagnetic fields decay sufficiently to zero, rather than terminating the lithosphere at a more shallow depth using an SIBC).

A2. Symmetrical 3-D FDTD Model Description

To reduce the computational running times, symmetrical 3-D FDTD models are used when possible. The running times for the symmetrical 3-D simulations average about two days while using 128 processors (half as long and half as many processors as the fully 3-D models). Figure 15 illustrates the symmetrical 3-D FDTD

grid. In this case, half of the grid is modeled compared to the fully 3-D model. The grid extends to ie cells in the x direction, to je cells in the y direction, and to ke cells in the z direction. In the y direction, there are half as many cells as in the fully 3-D model due to symmetry. The source is oriented along the x direction as in the 3-D model, and it is located along the axis of symmetry (a distance of one grid cell, Δz , from the edge of the grid in the y direction). Normal field updates are performed at the source and in the $+y$ direction from the source. The field values in the second grid cell in the y direction ($j = \text{second cell}$) are then copied to the first grid cell ($j = \text{first cell}$). CPML is used to terminate the symmetrical 3-D grid in the $\pm x$ directions as well as on the $+y$ side of the grid. The top and bottom edges of the grid (z direction) are terminated by an SIBC as for the fully 3-D model. Comparison of fully 3-D and symmetrical 3-D results yields identical results for cases wherein the geometry is symmetrical along the y direction away from the source. A symmetrical model may only be used if the model possesses symmetry in at least one direction. In the case of modeling 3-D objects with anisotropy in all three Cartesian directions, this symmetrical model may not be used.

A3. 2-D FDTD Model Description.

When the geometry can be considered homogeneous in one direction, and solutions for only three field components are needed, a 2-D FDTD model can be used. In this case, solutions along one plane of the grid cell (three different field components) are obtained. Referring to Figure 1, solutions are obtained for the fields on the front face of the grid cell (E_x , H_y , and H_z).

Acknowledgments

The authors thank the Extreme Science and Engineering Discovery Environment (XSEDE), which provided supercomputing resources through National Science Foundation grant number ACI-1105375, as well as the University of Utah's Center for High Performance Computing (CHPC). This work was also supported in part by a Blue Waters sustained-petascale computing project award 1440023, supported by the National Science Foundation (NSF) awards OCI-0725070 and ACI-1238993 and the State of Illinois. We would also like to thank R. Pirjola for sending us the analytical data used in Figure 3 to compare FDTD result with the analytical data. The data used for producing the figures in this paper are available from the authors upon request (santosh_everest@yahoo.com) or can be directly accessed from "The Hive: University of Utah Research Data Repository" using the link https://hive.utah.edu/concern/generic_works/0c483j36g. The authors thank Jennifer Gannon and one anonymous reviewer for their advice on this paper. This is also supported by NSF (National Science Foundation, 1662318).

References

- Bailey, R. C., & Edwards, R. N. (1976). The effect of source field polarization on geomagnetic variation anomalies in the British Isles. *Geophysical Journal of the Royal Astronomical Society*, 45(1), 97–104. <https://doi.org/10.1111/j.1365-246X.1976.tb00315.x>
- Bailey, R. L., Halbedl, T. S., Schattauer, I., Römer, A., Achleitner, G., Beggan, C. D., et al. (2017). Modelling geomagnetically induced currents in midlatitude Central Europe using a thin-sheet approach. *Annales de Geophysique*, 35(3), 751–761. <https://doi.org/10.5194/angeo-35-751-2017>
- Bannister, P. (1985). The determination of representative ionospheric conductivity parameters for ELF propagation in the Earth-ionosphere wave-guide. *Radio Science*, 20(4), 977–984. <https://doi.org/10.1029/RS020i004p00977>
- Beamish, D., Clark, T. D. G., Clarke, E., & Thomson, A. W. P. (2002). Geomagnetically induced currents in the UK: Geomagnetic variations and surface electric fields. *Journal of Atmospheric and Solar-Terrestrial Physics*, 64(16), 1779–1792. [https://doi.org/10.1016/S1364-6826\(02\)00127-X](https://doi.org/10.1016/S1364-6826(02)00127-X)
- Beggan, C. D., Beamish, D., Richards, A., Kelly, G. S., & Thomson, A. W. P. (2013). Prediction of extreme geomagnetically induced currents in the UK high-voltage network. *Space Weather*, 11, 407–419. <https://doi.org/10.1002/swe.2065>
- Beggs, J. H., Luebbers, R. J., Yee, K. S., & Kunz, K. S. (1992). Finite-difference time-domain implementation of surface impedance boundary conditions. *IEEE Transactions on Antennas and Propagation*, 40, 49–56. See also "Corrections," *IEEE Trans. Antennas Propagat.*, (Vol. 41, 1993, p. 118). <https://doi.org/10.1109/8.123352>
- Berenger, J.-P. (1994). A perfectly matched layer for the absorption of electromagnetic waves. *Journal of Computational Physics*, 114, 195–200.
- Bolduc, L. (2002). GIC observations and studies in the Hydro-Quebec power system. *Journal of Atmospheric and Solar: Terrestrial Physics*, 64(16), 1793–1802. [https://doi.org/10.1016/S1364-6826\(02\)00128-1](https://doi.org/10.1016/S1364-6826(02)00128-1)
- Boteler, D. H., & Pirjola, R. J. (1998). The complex-image method for calculating the magnetic and electric fields produced at the surface of the Earth by the auroral electrojet. *Geophysical Journal International*, 132, 31–40.
- Boteler, D. H., Pirjola, R. J., & Trichtchenko, L. (1999). On calculating the electric and magnetic fields produced in the technological systems at the Earth's surface by a "wide" electrojet. *Journal of Atmospheric and Solar-Terrestrial Physics*, 62, 1311–1315.
- British Geological Survey (2011). The largest magnetic storm on record, the "Carrington event" of August 27 to September 7, 1859, National Environment Research Council, retrieved March 28, 2009.
- Carrington, R. C. (1859). Description of a singular appearance seen in the Sun on September 1, 1859. *Monthly Notices of the Royal Astronomical Society*, 20, 13–15. <https://doi.org/10.1093/mnras/20.1.13>
- Chan, G. H., Dosso, H. W., & Law, L. K. (1981). An analogue model study of electromagnetic induction for cape and bay coastlines. *Physics of the Earth and Planetary Interiors*, 25(2), 167–176.
- Cliiverd, M. A., Rodger, C. J., Dietrich, S., Raita, T., Ulich, T., Clarke, E., et al. (2010). High-latitude geomagnetically induced current events observed on very low frequency radio wave receiver systems. *Radio Science*, 45, RS2006. <https://doi.org/10.1029/2009RS004215>
- Dawson, T. W., & Weaver, J. T. (1979). Three-dimensional induction in a non-uniform thin sheet at the surface of a uniformly conducting Earth. *Geophysical Journal of the Royal Astronomical Society*, 59(3), 445–462. <https://doi.org/10.1111/j.1365-246X.1979.tb02566.x>
- Dosso, H. W., Nienaber, W., & Hutton, V. R. S. (1980). An analogue model of electromagnetic induction in the British Isles. *Physics of the Earth and Planetary Interiors*, 22(1), 68–85. [https://doi.org/10.1016/0031-9201\(80\)90102-8](https://doi.org/10.1016/0031-9201(80)90102-8)
- Edwards, R. N., Law, L. K., & White, A. (1971). Geomagnetic variations in the British Isles and their relation to electrical currents in the oceans and shallow seas. *Royal Society of London*, A270, 289–232.
- Fernberg, P. (2012). One dimensional Earth resistivity models for selected areas of continental United States and Alaska, EPRI technical update, 1026430, Palo Alto, CA. Retrieved from <https://geomag.usgs.gov/conductivity/>
- Gilbert, J. L. (2005). Modeling the effect of the ocean-land interface on induced electric fields during geomagnetic storms. *Space Weather*, 3, S04A03. <https://doi.org/10.1186/S40623-015>
- Gilbert, J. L. (2014). Simplified techniques for treating the ocean-land interface for geomagnetically induced electric fields. In *2014 IEEE International Symposium on Electromagnetic Compatibility (EMC)* (pp. 566–569). Raleigh, NC.
- Gombosi, T. I., De Zeeuw, D. L., Groth, C. P. T., Powell, K. G., & Stout, Q. F. (2000). Multiscale MHD simulation of a coronal mass ejection and its interaction with the magnetosphere-ionosphere system. *Journal of Atmospheric and Solar: Terrestrial Physics*, 62(16), 1515–1525. [https://doi.org/10.1016/S1364-6826\(00\)00091-2](https://doi.org/10.1016/S1364-6826(00)00091-2)

- Green, V. R., & Weaver, J. T. (1978). Two-dimensional induction in a thin sheet of variable integrated conductivity at the surface of a uniformly conducting Earth. *Geophysical Journal International*, 55(3), 721–736. <https://doi.org/10.1111/j.1365-246X.1978.tb05939.x>
- Hakkinen, L., Pirjola, R., & Sucksdorff, C. (1989). EISCAT magnetometer cross and theoretical studies connected with electrojet current system. *Geophysica*, 25(1 & 2), 123–134.
- Hernance, J. F. (2013). Electrical Conductivity Models of the Crust and Mantle. In T. J. Ahrens (Ed.), *Global Earth Physics*. <https://doi.org/10.1029/RF001p0190>
- Hines, P. D. H., Dobson, I., & Rezaei, P. (2017). Cascading power outages propagate locally in an influence graph that is not the actual grid topology. *IEEE Transactions on Power Systems*, 32(2), 958–967.
- Kappenman, J. (2004). The evolving vulnerability of electric power grids. *Space Weather*, 2, S01004. <https://doi.org/10.1029/2003SW000028>
- Kappenman, J. (2010). Geomagnetic storms and their impacts on the U.S. power grid, Metatech Meta-R-319 Report prepared for Oak Ridge National Lab, Jan.
- Kraichman, M. B. (1977). Electromagnetic background noise in the ocean due to geomagnetic activity in the period range 0.5 to 1000 - seconds, Naval Surface Weapons Center, White Oak The Laboratory, Maryland.
- Matandirotya, E., Cilliers, P. J., Robert, R., & Zyl, V. (2015). Modeling geomagnetic induced currents in the South African power transmission network using the finite element method. *Space Weather*, 13, 185–195. <https://doi.org/10.1002/2014SW001135>
- McKay, A. J. (2004). Geoelectric fields and geomagnetically induced Currents in the United Kingdom, (PhD thesis). University of Edinburgh.
- Miles, T., & Dosso, H. W. (1980). An analogue model study of ocean-wave induced magnetic field variations near the coastline. *Journal of Geomagnetism and Geoelectricity*, 32, S1151–S1154. https://doi.org/10.5636/jgg.32.supplement1_S1151
- National Research Council of the National Academies (2008). Severe space weather events—Understanding societal and economic impacts, A Workshop Report, Washington, DC, May.
- Ngwira, C. M., Pulkkinen, A. A., Bernabeu, E., Eichner, J., Viljanen, A., & Crowley, G. (2015). Characteristics of extreme geoelectric fields and their possible causes: Localized peak enhancements. *Geophysical Research Letters*, 42, 6916–6921. <https://doi.org/10.1002/2015GL065061>
- Nickolaenko, A., Galuk, Y., & Hayakawa, M. (2016). Vertical profile of atmospheric conductivity that matches Schumann resonance observations. *Springerplus*, 5(1), 108. <https://doi.org/10.1186/s40064-016-1742-3>
- Odenwald, S. (2002). *The 23rd cycle: Learning to live with a stormy star*. Columbia University Press. <https://doi.org/10.7312/oden12078>
- Oijala, P., Markkanen, J., Jarvenpaa, S., & Kiminki, S. P. (2014). Surface and volume integral methods for time-harmonic solutions of Maxwell's equations.
- Olsen, N., & Kuvshinov, A. (2004). Modeling the ocean effect of geomagnetic storms. *Earth, Planets and Space*, 56, 523–530.
- Pirjola, R. (2013). Practical model applicable to investigating the coast effect on the geoelectric field in connection with studies of geomagnetically induced currents. *Advances in Applied Physics*, 1(1), 9–28. <https://doi.org/10.12988/aap.2013.13002>
- Powell, K. G., Roe, P. L., Linde, T. J., Gombosi, T. I., & De Zeeuw, D. L. (1999). A solution-adaptive upwind scheme for ideal magnetohydrodynamics. *Journal of Computational Physics*, 154(2), 284–309. <https://doi.org/10.1006/jcph.1999.6299>
- Pulkkinen, A., Bernabeu, E., Eichner, J., Viljanen, A., & Ngwira, C. (2015). Regional-scale high-latitude extreme geoelectric fields pertaining to geomagnetically induced currents. *Earth, Planets and Space*, 67(1), 93. <https://doi.org/10.1186/s40623-015-0255-6>
- Pulkkinen, A., Hesse, M., Kuznetsova, M., & Rastatter, L. (2007). First principles modeling of geomagnetically induced electromagnetic fields and currents from upstream solar wind to the surface of the Earth. *Annales Geophysicae*, 25(4), 881–893. <https://doi.org/10.5194/angeo-25-881-2007>
- Püthe, C., Manoj, C., & Kuvshinov, A. (2014). Reproducing electric field observations during magnetic storms by means of rigorous 3-D modelling and distortion matrix co-estimation. *Earth, Planets and Space*, 66(1), 162. <https://doi.org/10.1186/s40623-014-0162-2>
- Richmond, A. D. (1992). Assimilative mapping of ionospheric electrodynamics. *Advances in Space Research*, 12(6), (6)59–(6)68. [https://doi.org/10.1016/0273-1177\(92\)90040-5](https://doi.org/10.1016/0273-1177(92)90040-5)
- Roden, J. A., & Gedney, S. D. (2000). Convolutional PML (CPML): An efficient FDTD implementation of the CFS-PML for arbitrary media. *Microwave and Optical Technology Letters*, 27(5), 334–339. [https://doi.org/10.1002/1098-2760\(20001205\)27:5%3C334::AID-MOP14%3E3.0.CO;2-A](https://doi.org/10.1002/1098-2760(20001205)27:5%3C334::AID-MOP14%3E3.0.CO;2-A)
- Samimi, A., & Simpson, J. J. (2016). Parallelization of 3-D Global FDTD Earth-Ionosphere Waveguide Models at Resolutions on the Order of –1 km and Higher. In *IEEE Antennas and Wireless Propagation Letters* (Vol. 15, pp. 1959–1962). <https://doi.org/10.1109/LAWP.2016.2545526>
- Sevgi, L., Akleman, F., & Felsen, L. B. (2002). Groundwave propagation modeling: Problem-matched analytical formulations and direct numerical techniques. *IEEE Antennas and Propagation Magazine*, 44(1), 55–75. <https://doi.org/10.1109/74.997903>
- Shepard, S. G., & Shubitidze, F. (2003). Method of auxiliary sources for calculating the magnetic and electric fields induced in a layered Earth. *Journal of Atmospheric and Solar-Terrestrial Physics*, 65(10), 1151–1160. [https://doi.org/10.1016/S1364-6826\(03\)00159-7](https://doi.org/10.1016/S1364-6826(03)00159-7)
- Simpson, J. J. (2011). On the possibility of high-level transient coronal mass ejection-induced ionospheric current coupling to electric power grids. *Journal of Geophysical Research*, 116, A11308. <https://doi.org/10.1029/2011JA016830>
- Simpson, J. J., & Taflove, A. (2004). Three-dimensional FDTD modeling of impulsive ELF propagation about the Earth-sphere. *IEEE Transactions on Antennas and Propagation*, 52(2), 443–451. <https://doi.org/10.1109/TAP.2004.823953>
- Simpson, J. J., & Taflove, A. (2006). A novel ELF radar for major oil deposits. *IEEE Geoscience and Remote Sensing Letters*, 3(1), 36–39. <https://doi.org/10.1109/LGRS.2005.856118>
- Taflove, A., & Hagness, S. C. (2005). *Computational electrodynamics: The finite-difference time-domain method* (3rd ed.). Norwood, MA: Artech House.
- Thomson, A. W. P., McKay, A. J., Clarke, E., & Reay, S. J. (2005). Surface electric fields and geomagnetically induced currents in the Scottish Power grid during the 30 October 2003 geomagnetic storm. *Space Weather*, 3, S11002. <https://doi.org/10.1029/2005SW000156>
- Torta, J. M., Marcuello, A., Campaña, J., Marsal, S., Queralt, P., & Ledo, J. (2017). Improving the modeling of geomagnetically induced currents in Spain. *Space Weather*, 15, 691–703. <https://doi.org/10.1002/2017SW001628>
- Vasseur, G., & Weidelt, P. (1977). Bimodal electromagnetic induction in non-uniform thin sheets with an application to the northern Pyrenean induction anomaly. *Geophysical Journal of the Royal Astronomical Society*, 51, 669–690. <https://doi.org/10.1111/j.1365-246X.1977.tb04213.x>
- Viljanen, A., Pulkkinen, A., Pirjola, R., Pajunpää, K., Posio, P., & Koistinen, A. (2006). Recordings of geomagnetically induced currents and a nowcasting service of the Finnish natural gas pipeline system. *Space Weather*, 4, S10004. <https://doi.org/10.1029/2006SW000234>
- Wei, H. L., Homeier, N., & Gannon, J. L. (2013). Surface electric fields for North America during historical geomagnetic storms. *Space Weather*, 11, 451–462. <https://doi.org/10.1002/swe.20073>
- Yee, K. S. (1966). Numerical solution of initial boundary value problems involving Maxwell's equations in isotropic media. *IEEE Transactions on Antennas and Propagation*, 14, 302–307.